Weighted essential non-oscillatory schemes for tidal bore on unstructured meshes

Changna Lu[1,2], Jianxian Qiu[3, *, †] and Ruyun Wang[1]

[1]*State Key Laboratory of Hydrology-Water Resources and Hydraulic Engineering, Hohai University, Nanjing, Jiangsu 210098, People's Republic of China*
[2]*College of Ocean, Hohai University, Nanjing, Jiangsu 210098, People's Republic of China*
[3]*Department of Mathematics, Nanjing University, Nanjing, Jiangsu 210093, People's Republic of China*

SUMMARY

In this paper, the third-order weighted essential non-oscillatory (WENO) schemes are used to simulate the two-dimensional shallow water equations with the source terms on unstructured meshes. The balance of the flux and the source terms makes the shallow water equations fit to non-flat bottom questions. The simulation of a tidal bore on an estuary with trumpet shape and Qiantang river is performed; the results show that the schemes can be used to simulate the current flow accurately and catch the stronger discontinuous in water wave, such as dam break and tidal bore effectively. Copyright © 2008 John Wiley & Sons, Ltd.

1. INTRODUCTION

In this paper, the weighted essential non-oscillatory (WENO) schemes are used to simulate the tidal bore of the two-dimensional shallow water equations for Qiantang river on unstructured triangle meshes.

There are many rivers that have tidal bore in the world, such as Amazon in South America, Seine river in French, and so on. But the tidal bore in Qiantang river is greater and worth considering.

*Correspondence to: Jianxian Qiu, Department of Mathematics, Nanjing University, Nanjing, Jiangsu 210093, People's Republic of China.
†E-mail: jxqiu@nju.edu.cn

Qiantang river lies in the south of Shanghai, China, which is very famous for high tidal bore. Although tidal bore is one of the important reasons that make disaster to those regions along Qiantang river about every five years, it damages the dykes and dams mainly. To efficiently control the danger of the tidal bore and keep the sight, it is necessary to understand the process of tidal bore more. Numerical simulation is an important way except the physical model, and the complexity of the shape of the gulf and the topography of the bottom surface need numerical methods with higher precision.

As we know, the performance of the shallow water equations without the source terms is similar to that of the compressible Euler equations in aerodynamics. A lot of shock and discontinuity capture methods that are well developed in aerodynamics can be used to solve the shallow water equations, including the cases with strong discontinuity, such as tidal bore. In [1, 2] the finite difference methods were adopted to solve the shallow water equations, and these methods were based on rectangular meshes; they could not approximate the boundary accurately in bays and estuaries that have complex geometries. In fact, the finite element methods [3] are convenient for questions with complex geometries; however, in these methods the established algebraic equations are non-linear and have to be solved by the iteration process. Moreover, the boundary conditions and the mesh structures have a great influence on the numerical results. The finite volume methods are widely used as they have the merits of the finite difference methods and the finite element methods. In recent years, high-resolution finite volume methods for hyperbolic systems of conservation laws have been extensively applied to solve the shallow water equations. In particular, the finite volume methods of the Godunov class are quite mature and can be used in different practical engineering applications. In most of the applications, second-order accuracy schemes were used, as it is the optimal compromise between a reasonable mesh refinement and an acceptable complexity of numerical schemes.

The WENO schemes are a very important class of high-accuracy numerical methods [4, 5]. The WENO is a procedure of spatial discretization, namely, it is a procedure to approximate the spatial derivative terms. The WENO schemes use the idea of adaptive stencils in the reconstruction procedure based on the local smoothness of the numerical solution to automatically achieve high-order accuracy and a non-oscillatory property near discontinuities. The WENO methods have been developed in recent years as a class of high-order methods for conservation laws, which give sharp, non-oscillatory discontinuity transitions and at the same time provide high-order accurate resolutions for the smooth part of the solution.

There are several papers that studied tidal bore, such as Su *et al.* [6] established a one-dimensional model from Ganpu to Fuchun station, and a two-dimensional model covering the local area from Ganpu to Yanguan station for Qiantang river. They simulated a tidal event and compared it with the observed tidal elevations in Qiantang river, and they used a new non-oscillatory and non-free dissipation parameter difference scheme to simulate the full process. Pan *et al.* [7] used the Godunov-type schemes with the water level-bottom topography formulation to simulate the formation, evolution and dissipation of the tidal bore in Qiantang river. Hui and Pan [8] established a two-dimensional flexible meshes models for Qiantang river. Madsen *et al.* [9] developed an implicit finite difference formulation of the shallow water equations to treat tidal bore and hydraulic jumps. The accuracies of those schemes are not more than second order.

If the source terms are ignored, the systems of the shallow water equations are homogeneous. However, the inclusion of the source terms, which differ from Euler equations, makes the model more complex, the source terms relevant to bed topography, bed shear stress and Coriolis term. Essentially, a numerical imbalance is created by the artificial splitting to generate a mathematical

hyperbolic formulation. These terms are evaluated by different methods at different locations within the computational meshes creating numerical imbalance. Many numerical solvers of the shallow water equations give unphysical results for flow over physically realistic variable bathymetry, solely because of this mathematically convenient splitting. The study for solving the full shallow water equations receives attentions continuously. Recently, various researchers have developed new methods for the shallow water equations with the source terms. For example, LeVeque [10] developed a treatment for the bed slope source terms, which balanced the source terms and the flux gradients, but the method for quasi-steady problems is reported to be less successful when applied to calculate steady flow with a shock. Hubbard and Garcia-Navarro [11] used numerical upwind of the source terms to achieve equilibrium between the flux gradient and the source terms in the shallow water equations with higher-order total variation diminishing (TVD) schemes. Meanwhile, Zhou *et al.* [12] suggested an alternative piecewise linear reconstruction of the surface gradient term in the shallow water equations, which was demonstrated using an HLL Riemann solver.

In this paper, the third-order WENO schemes are used to solve the tidal bore of the two-dimensional shallow water equations with the source terms on unstructured triangle meshes. We follow the ideas of Hu and Shu [13] about the WENO schemes and Rogers *et al.* [14] about the balance of the flux and the source terms. We consider the case of flow over wet non-flat bed. This paper is organized as follows. In Section 2, we describe the property and discretization of the shallow water equations by the third-order WENO schemes. Numerical examples and applications are given to demonstrate the accuracy and the resolution of the constructed schemes in Section 3. Concluding remarks are included in Section 4.

2. DESCRIPTION OF NUMERICAL MODEL AND NUMERICAL METHOD

2.1. The governing equations

The two-dimensional conservative unsteady shallow water equations are

$$U_t + F(U)_x + G(U)_y = H \tag{1}$$

with

$$U = [D, uD, vD]^{\mathrm{T}}, \quad F(U) = [uD, u^2 D + gD^2/2, uvD]^{\mathrm{T}}, \quad G(U) = [vD, uvD, v^2 D + gD^2/2]^{\mathrm{T}}$$

and the source terms

$$H = [0, Dfv - gDS_{ox} + (\tau_{ax} - \tau_{bx})/\rho, -Dfu - gDS_{oy} + (\tau_{ay} - \tau_{by})/\rho]^{\mathrm{T}} \tag{2}$$

where D is the total water depth; u and v are the depth-averaged velocities in the x- and y-directions, respectively; t is the time; g is the gravitational acceleration; ρ is the water density; τ_{ax} and τ_{ay} are the surface stresses, τ_{bx} and τ_{by} are the bed friction stresses; S_{ox} and S_{oy} are the bed slopes stresses, $S_{ox} = \partial b/\partial x$, $S_{oy} = \partial b/\partial y$, b is the bottom function; and f is the Coriolis parameter. The bed friction stress in the x- and y-directions is calculated by Manning formulations:

$$\tau_{bx} = -g\frac{n^2 u\sqrt{u^2 + v^2}}{D^{1/3}}, \quad \tau_{by} = -g\frac{n^2 v\sqrt{u^2 + v^2}}{D^{1/3}} \tag{3}$$

respectively, where n denotes Manning's roughness coefficient.

We express the shallow water equations in quasi-linear form as follows:

$$U_t + A(U)U_x + B(U)U_y = H \tag{4}$$

where

$$A(U) = \frac{\partial F}{\partial U} = \begin{pmatrix} 0 & 1 & 0 \\ c^2 - u^2 & 2u & 0 \\ -uv & v & u \end{pmatrix}, \quad B(U) = \frac{\partial G}{\partial U} = \begin{pmatrix} 0 & 0 & 1 \\ -uv & v & u \\ c^2 - v^2 & 0 & 2v \end{pmatrix} \tag{5}$$

and $c = \sqrt{gD}$ is the propagation speed of the shallow water wave. The eigenvalues of A and B are

$$\lambda(A) = u + c, u, u - c, \quad \lambda(B) = v + c, v, v - c$$

respectively.

2.2. Description of the third-order WENO schemes

We solve the shallow water equations using the finite volume formulation. The computational control volumes are unstructured triangle meshes.

Taking the triangle $\triangle_0$ as the control volume, let $\mathbf{F} = (F, G)$, we formulate the semi-discrete finite volume scheme of Equations (1) as

$$\frac{\mathrm{d}}{\mathrm{d}t} \int_{\triangle_0} U \, \mathrm{d}\triangle = -\sum_{k=1}^{3} \int_{L_k} \mathbf{F} \cdot \mathbf{n}_k \, \mathrm{d}l + \int_{\triangle_0} H \, \mathrm{d}\triangle \tag{6}$$

where $L_k(k = 1, 2, 3)$ is the kth edge of triangle $\triangle_0$, $\mathbf{n}_k$ is the outward unit normal of the L_k. The mean value of U and H on the cell $\triangle_0$ is defined as

$$\bar{U}_0 = \frac{1}{|\triangle_0|} \int_{\triangle_0} U \, \mathrm{d}\triangle, \quad \bar{H}_0 = \frac{1}{|\triangle_0|} \int_{\triangle_0} H \, \mathrm{d}\triangle \tag{7}$$

The line integral in Equation (6) is discretized by a q-point Gaussian quadrature

$$\int_{L_k} \mathbf{F} \cdot \mathbf{n}_k \, \mathrm{d}l \approx |L_k| \sum_{j=1}^{q} \omega_j \mathbf{F}(U(G_j, t)) \cdot \mathbf{n}_k \tag{8}$$

$\mathbf{F}(U(G_j, t))$ is replaced by a numerical flux $\mathbf{F}^*$. Here, the simple Lax–Friedrich flux is used, which is given by

$$\mathbf{F}^*(U_j^+, U_j^-) \cdot \mathbf{n} = \tfrac{1}{2}[(\mathbf{F}(U^-(G_j, t)) + \mathbf{F}(U^+(G_j, t))) \cdot \mathbf{n} - \alpha(U^+(G_j, t) - U^-(G_j, t))] \tag{9}$$

where α is taken as an upper bound for the absolute value of eigenvalues in the n direction for the Jacobian matrices $A(U)$ and $B(U)$, and $U^-(G_j, t)$ and $U^+(G_j, t)$ are the values of U inside the cell $\triangle_0$ and outside the cell $\triangle_0$ (inside the neighboring cell) at the Gaussian point G_j.

We are constructing schemes up to third-order accuracy for reconstruction of $U^\pm(G_j, t)$; the two-point Gaussian quadrature is used, which has $G_1 = \alpha P_1 + (1 - \alpha)P_2$, $G_2 = (1 - \alpha)P_1 + \alpha P_2$, $\alpha = \frac{1}{2} + \frac{\sqrt{3}}{6}$ and $\omega_1 = \omega_2 = \frac{1}{2}$ for the line with endpoints P_1 and P_2.

The present numerical schemes follow the ideas of the WENO schemes in the paper of Hu and Shu [13]. In order to obtain higher-order accuracy in the WENO schemes on triangle cells when
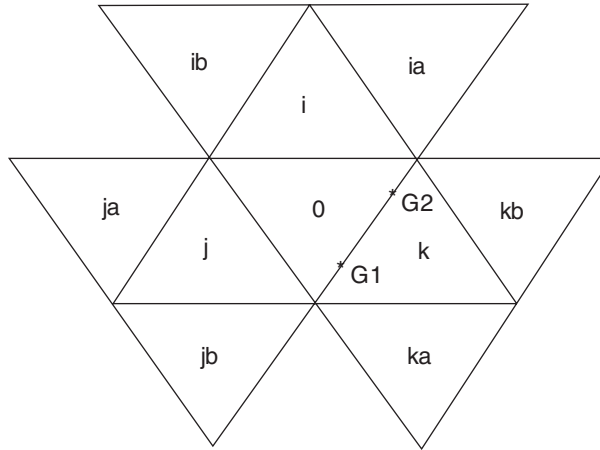
Figure 1. A typical stencil.

using the same set of the ENO stencils, first we need a quadratic polynomial reconstruction of p^2, which requires that it has the same cell average as U on triangle $\triangle_0$ and it matches the cell averages of U on the nine neighbor cells of $\triangle_0$ in a least-squares sense (see Figure 1, let $\triangle_i, \triangle_j, \triangle_k$ be its three neighbors, and $\triangle_{ia}, \triangle_{ib}$, be the two neighbors (other than $\triangle_0$) of $\triangle_i$, and so on). Then we need to construct several linear polynomials $p_s(x,y)(s=1,2,\ldots,9)$ whose weighted average will give the same result as the quadratic reconstructions p^2 at each quadrate point:

$$R(x,y) = \sum_{s=1}^{9} \gamma_s p_s(x,y) \tag{10}$$

$$R(x^G, y^G) = p^2(x^G, y^G) \tag{11}$$

where $p_s(x,y)(s=1,2,\ldots,9)$ are the linear polynomials in agreement with the cell average of U on the nine stencils: $S_1 = \{\triangle_0, \triangle_j, \triangle_k\}$, $S_2 = \{\triangle_0, \triangle_k, \triangle_i\}$, $S_3 = \{\triangle_0, \triangle_i, \triangle_j\}$, $S_4 = \{\triangle_0, \triangle_i, \triangle_{ia}\}$, $S_5 = \{\triangle_0, \triangle_i, \triangle_{ib}\}$, $S_6 = \{\triangle_0, \triangle_j, \triangle_{ja}\}$, $S_7 = \{\triangle_0, \triangle_j, \triangle_{jb}\}$, $S_8 = \{\triangle_0, \triangle_k, \triangle_{ka}\}$, $S_9 = \{\triangle_0, \triangle_k, \triangle_{kb}\}$.

We can obtain 10 linear equations for the nine weights γ_s. $R(x,y)$ as a linear polynomial has the same order with quadratic polynomial p^2 on every Gaussian point. In order to ensure stability near shocks, we need non-negative weights, and grouping of polynomials is used to achieve positivity:

$$\sum_{s=1}^{3} \tilde{\gamma}_s \tilde{p}_s(x,y) = \sum_{s=1}^{9} \gamma_s p_s(x,y) \tag{12}$$

The resultant linear polynomial

$$\tilde{R}(x,y) = \sum_{s=1}^{3} \tilde{\gamma}_s \tilde{p}_s(x,y) \tag{13}$$

is identical to $R(x,y)$ in (10) and in most cases the coefficients $\tilde{\gamma}_s$ can be made non-negative.

The last is to compute the smoothness indicators and the non-linear weights. In this paper, for a polynomial $p(x, y)$ with degree up to k, we select the following measurement for smoothness, as defined in [13]:

$$\mathrm{IS} = \sum_{1 \leqslant |\alpha| \leqslant k} \int_{\triangle} |\triangle|^{|\alpha|-1} (D^{\alpha} p(x, y))^2 \, \mathrm{d}x \, \mathrm{d}y \tag{14}$$

where α is a multi-index and D is the derivative operator. The indices of smoothness are used inside the final expressions for the weights:

$$\omega_k = \frac{\varpi_k}{\sum \varpi_j}, \quad \varpi_k = \frac{\gamma_k}{(\varepsilon + IS_k)^2} \tag{15}$$

where γ_k is the kth coefficient in the linear combination of polynomials (i.e. the $\tilde{\gamma}_k$ in (13)). ε is a small positive constant used to avoid the denominator to become zero and is typically taken as 10^{-6}; and IS_k are the so-called 'smoothness indicators', which measure the smoothness of the polynomials. The non-linear weights ω_k would replace the linear weights γ_s to form the WENO reconstruction.

With the numerical flux F^*, $F(U)$ is approximated by (9) to higher-order accuracy at Gaussian points.

The semi-discrete scheme (6), expressed as

$$U_t = L(U)$$

is discretized in time by a TVD Runge–Kutta method [15], for example, the third-order version given by

$$
\begin{aligned}
U^{(1)} &= U^n + \triangle t L(U^n) \\
U^{(2)} &= \tfrac{3}{4} U^n + \tfrac{1}{4} U^{(1)} + \tfrac{1}{4} \triangle t L(U^{(1)}) \\
U^{n+1} &= \tfrac{1}{3} U^n + \tfrac{2}{3} U^{(2)} + \tfrac{2}{3} \triangle t L(U^{(2)})
\end{aligned}
\tag{16}
$$

2.3. Balance of the flux and the source terms

Here we adopt the ideas of Rogers *et al.* [14] about the balance of the flux and the source terms; they presented an algebraic technique for balancing the flux gradients and the source terms in finite volume schemes. The numerical imbalance is eradicated by reformulating the governing matrix hyperbolic system of conservation laws in terms of deviations away from an unforced but separately specified equilibrium state. Thus, balancing is achieved by the incorporation of this extra physical information and bypasses conventional numerical treatments of the imbalance.

The vector of conserved variables U is given by

$$U = U^{\mathrm{eq}} + U' \tag{17}$$

where U' is the deviation of U from the equilibrium or still water value such that $\partial U^{\mathrm{eq}}/\partial t = 0$. In fact, for still water values, the shallow water convenient properties $\zeta = u = v = 0$, and

$$U^{\mathrm{eq}} = [h, 0, 0]^{\mathrm{T}}, \quad U' = U - U^{\mathrm{eq}} = [\zeta, uD, vD]^{\mathrm{T}}$$

where ζ is the free surface elevation above the still water level h, and $D = \zeta + h$ is the total water depth. The shallow water equations are transformed to

$$\frac{\partial U'}{\partial t} + \frac{\partial [F(U) - F(U^{\text{eq}})]}{\partial x} + \frac{\partial [G(U) - G(U^{\text{eq}})]}{\partial y} = H - \frac{\partial (F(U^{\text{eq}}))}{\partial x} - \frac{\partial (G(U^{\text{eq}}))}{\partial y} \quad (18)$$

$$U'_t + F'(U)_x + G'(U)_y = H' \quad (19)$$

with

$$U' = [\zeta, uD, vD]^{\text{T}}, \quad F' = [uD, u^2 D + g(\zeta^2 + 2h\zeta)/2, uvD]^{\text{T}}$$

$$G' = [vD, uvD, v^2 D + g(\zeta^2 + 2h\zeta)/2]^{\text{T}} \quad (20)$$

$$H' = [0, Dfv - g\zeta S_{ox} + (\tau_{ax} - \tau_{bx})/\rho, -Dfu - g\zeta S_{oy} + (\tau_{ay} - \tau_{by})/\rho]^{\text{T}}$$

We can see that the Jacobian matrixes $A'(U)$ and $B'(U)$ of (19) are the same as $A(U)$ and $B(U)$ of (1), and the discretization of Equations (19) is similar to that of (1).

The approach taken in the paper for some examples chosen is to use the still water level as the datum h. It is perfectly reasonable to choose a fixed horizontal datum elsewhere and derive the balanced hyperbolic equations using a stage-discharge approach.

3. NUMERICAL RESULTS

In this section, we perform numerical experiments to test the performance of the WENO schemes for the two-dimensional shallow water equations on unstructured triangle meshes, and then we used the methods to simulate tidal bore on an estuary with trumpet shape and Qiantang river.

In our numerical experiments, the surface stresses and the Coriolis are ignored; the gravitation constant is taken as $9.8 \, \text{m/s}^2$; Manning's roughness coefficient n is taken as 0.0001 except for the test of Qiantang river; the small positive constant in the WENO weight formula is taken as $\varepsilon = 10^{-6}$.

3.1. Test for the exact C-property

In this test case [16, 17], the bottom is defined as

$$b(x, y) = 0.8 \exp(-50((x - 0.5)^2 + (y - 0.5)^2)) \quad x, y \in [0, 1]$$

The initial water level is defined as $D(x, y) = 1 - b(x, y)$, and the initial velocity is defined as zero. The surface should remain flat. The terminal time is taken as $t = 0.1$.

We take the still level h as $h = 1 - b(x, y)$. In Table I, L^1 and L^∞ are the errors of water level D and the discharge Du and Dv when the *Courant–Friedrichs–Lewy* (CFL) number is 0.3 and 0.6, respectively, l is the average length of the sides. There are meshes of 216, 884 and 16 804 unstructured triangle cells that correspond to $l = 0.1, 0.05, 0.015$, respectively. We remark that l here is only a rough indicator of the mesh size. The results obviously confirm the theoretical result of the proposition basically. The accuracy is good.

3.2. *Test for the orders of accuracy*

To check the numerical order of accuracy, we use the same test as in [16]. On the unit square $[0, 1] \times [0, 1]$, we choose the bottom topography to be

$$b(x, y) = \sin(2\pi x) + \cos(2\pi y)$$

the initial data are given by

$$D(x, y, 0) = 10 + e^{\sin(2\pi x)} \cos(2\pi y)$$

$$Du(x, y, 0) = \sin(\cos(2\pi x)) \sin(2\pi y)$$

$$Dv(x, y, 0) = \cos(2\pi x) \cos(\sin(2\pi y))$$

We take the still level h as $h = 10 - b(x, y)$. We compute up to time $t = 0.05$ when there is no shock in the solution, with periodic boundary conditions. We use structured and central axially

Table I. Accuracy for the stationary solution.

l	CFL	D		Du		Dv	
		L^1	L^∞	L^1	L^∞	L^1	L^∞
0.015	0.3	4.885E−15	2.817E−15	1.508E−14	1.169E−14	1.297E−14	9.465E−15
	0.6	6.439E−15	3.973E−15	6.710E−14	6.707E−14	3.836E−14	3.835E−14
0.05	0.3	4.441E−16	3.552E−16	1.089E−15	8.492E−16	4.886E−16	4.816E−16
	0.6	4.441E−16	4.423E−16	1.033E−15	9.403E−16	7.148E−16	6.654E−16
0.1	0.3	3.775E−15	1.685E−15	1.503E−14	6.258E−15	3.555E−15	1.863E−15
	0.6	6.439E−15	2.733E−15	1.951E−14	7.759E−15	4.441E−15	2.184E−15
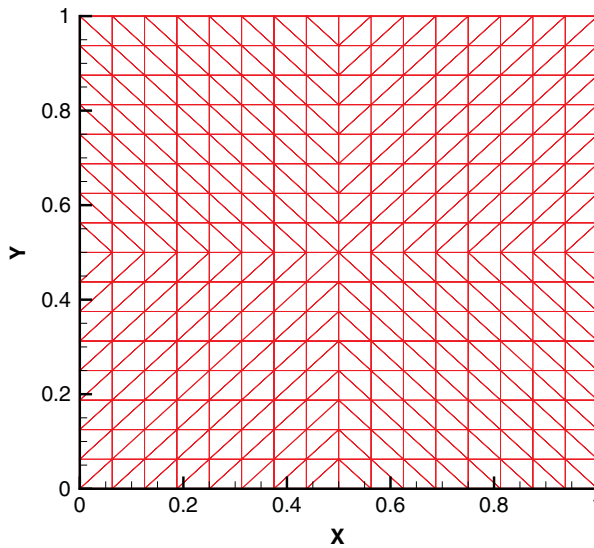
Figure 2. Meshes of the test for the orders of accuracy.

Table II. L^1 errors and numerical orders of accuracy for the order test.

	D		Du		Dv	
N	L^1 error	Order	L^1 error	Order	L^1 error	Order
16	1.941E−1		3.311E−1		2.532E−1	
32	3.252E−2	2.58	5.976E−2	2.47	4.216E−2	2.59
64	4.465E−3	2.86	8.435E−3	2.82	6.198E−3	2.77
128	5.864E−4	2.93	1.091E−3	2.95	8.274E−4	2.91
256	7.560E−5	2.96	1.387E−4	2.97	1.071E−4	2.95

symmetric triangle meshes as the periodic boundary conditions (see in Figure 2). The reference solution is computed with the same scheme and 512 cells in the x direction, since the exact solution is unknown.

In Table II, the L^1 errors of water level D and the discharge Du and Dv are displayed when the *CFL* number is 0.3, N is the cells' number in the x direction. We can see that the third-order accuracy is achieved for the finite volume WENO schemes.

3.3. A small perturbation of steady-state water

This is a classical example to show the capability of the proposed scheme for the perturbation of the stationary state [10, 14]. The computational domain is $[0, 2] \times [0, 1]$, and the bottom topography is given by the function

$$b(x, y) = 0.8 \exp(-5(x - 0.9)^2 - 50(y - 0.5)^2) \quad x, y \in [0, 2] \times [0, 1]$$

The surface is initially given by

$$D(x, y) = \begin{cases} 1 - b(x, y) + 0.01, & 0.05 \leqslant x \leqslant 0.15 \\ 1 - b(x, y) & \text{otherwise} \end{cases}, \quad u(x, y, 0) = v(x, y, 0) = 0$$

The absorbing extrapolation boundary conditions of the left and right boundaries are used, and the reflection boundary condition is used for up and down solid wall boundaries.

We take the still level h as $h = 1 - b(x, y)$. Figure 3 displays the right-going disturbance as it propagates the hump on a mesh of 16 804 unstructured triangle cells and 8585 vertexes divided by surface-water modeling system. The contours of the surface level $D + b$ are presented at different times. The results are in agreement with other results and indicate that our scheme can resolve the complex small features of the flow very well.

3.4. Asymmetric break of dam

We consider the sudden break of a dam separating two basins with the surface level of 5 m (downstream) and 10 m (upstream). The dam breaks asymmetrically at time $t = 0$. We simulate the test case until time $t = 7.2$. The length of the breach is 75 and it starts at $y = 95$. Reflection boundary conditions are applied on all the edges of the domain. Figure 4 shows the description of the test case. A mesh of unstructured triangle 17 658 cells with 8945 vertexes is used, and the average length of the sides is 2.2.
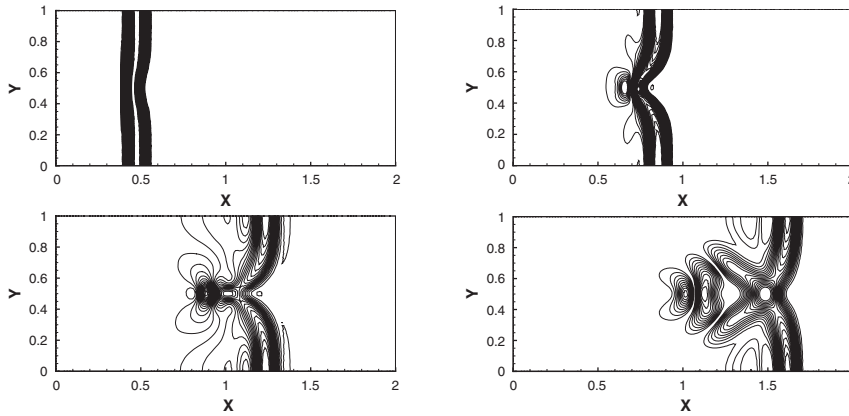
Figure 3. The contours of the surface level $D+b$ of steady-state water. Thirty uniformly spaced contour lines at time $t=0.12$ (top left), at time $t=0.24$ (top right), at time $t=0.36$ (bottom left), at time $t=0.48$ (bottom right).
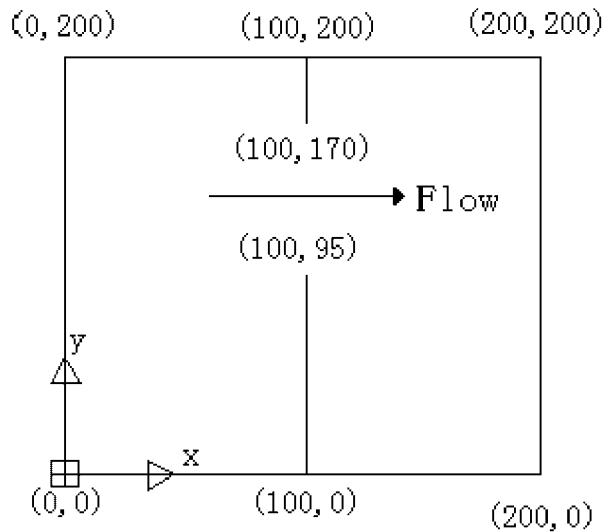

Figure 4. The description of dam break.

The contours of the surface level and velocity vectors are shown in Figures 5 and 6. We can see in the figures that the right moving flow propagates to the downstream up and down, and rarefaction wave propagates to the upstream; two asymmetric spiral vortexes are formed on both sides of the breach because of the great velocity and the reflection of the wave on the upper wall. Our results are similar to other results presented in the literature greatly, e.g. [17–19].

3.5. Tidal bore of an estuary with trumpet shape

In this section, we present some results obtained on an estuary with trumpet shape of flat bottom. Here we make a generalized stream channel whose shape is like a trumpet (Figure 7), which
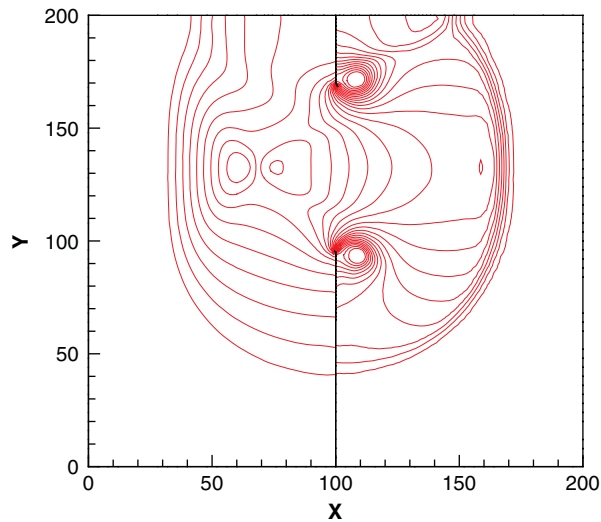
Figure 5. The contours of the surface level for dam break (25 levels from 4.0 to 9.6).
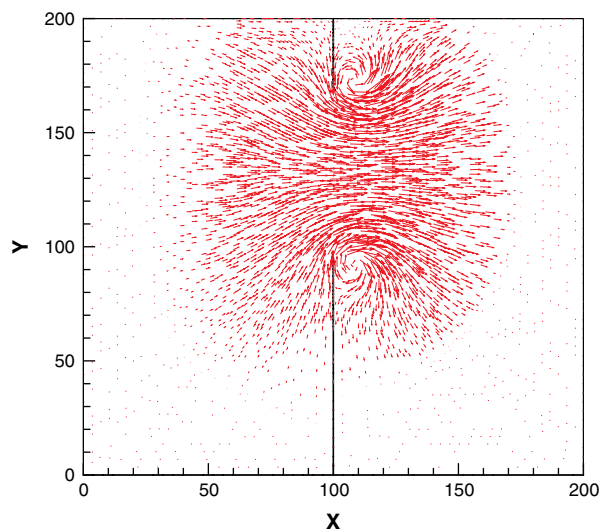
Figure 6. Velocity vectors at time $t = 7.2$ for dam break.

determines the formation of tidal bore. The total length is 300 km. The first 100 km length from zero is the shrinkage of the trumpet with the greatest width 120 km at zero as downstream. The next 200 km length is straight with the same width of 4 km. The flow is calculated on a mesh of unstructured triangle 4060 cells and 2303 vertexes; the least scale of elements is about 0.5 km, and the biggest scale is about 3 km. The initial velocity and the free surface elevation above the still water level are set to be zero as the initial conditions. We take the depth of the still water level as 10 m and the simple harmonic wave with a tide range of 4 m and periodic time of 12 h (like
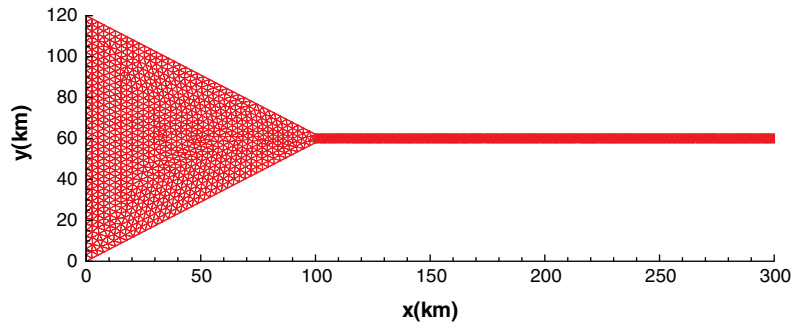
Figure 7. Shape and meshes of a trumpet estuary.

$M2$ component tide) as the periodic water boundary condition for downstream (east boundary). The absorbing extrapolation boundary condition for upstream is used, and the reflection boundary condition is used for solid wall boundary.

We calculate at three periodic intervals, and the total time is 36 h. When flow propagates to the straight channel, the tidal bore is formed, which is caused by the shrinking open mouth, but not clear. After cumulative 25 h, the tidal bore is very explicit. The surface level in three dimensions is shown in Figure 8 from cumulative $t = 25$ to 32 h from top to bottom. In those figures, when the tide comes into the straight channel, firstly, the water level rises greatly. The difference between the left and right of the tidal is enlarged, the tidal bore is formed, and then the height of the tidal bore is enlarged gradually until it is more than 4 m. From $t = 28$, the tidal bore is just like a wall, which propagates to upstream, and the height of the wall increases until $t = 23$, when the tidal bore almost runs out of the channel. The figures describe the propagation of tidal bore to the upstream with a speed of about 5 m/s.

Figure 9 shows the distribution of water level with 360 data at $x = 0$, 50, 100, 150, 200, 250, and 300 km, respectively. We note that the mean water level rises greatly. The shape of time series changes from almost sinusoidal to a very asymmetrical shape with an almost abrupt increase in water level. During the first 100 km, the amplitude of a simple harmonic wave (tidal range) increased gradually, while decreased little by little when it propagates to upstream into the straight channel, and the shape of the wave is distorted, and flood tide following the tidal bore duration reduced continuously. Tidal bore has formed at $x = 150$ km; then the tidal bore height enlarges continually until it is equal to the tidal range approximately.

3.6. Tidal bore of Qiantang river

The shape of the Qiantang river looks like a trumpet. The computational domain of the Qiantang river is from Ganpu with 22 km width to Zhakou with 2 km width over a distance of 102 km, the estuary has a dramatic decrease in width, and it amplifies the tidal range significantly. The seawater from the east adjacent to East China Sea flows into Qiantang coastal at the inlet; the mouth is wide, water has to surge more and more as its flow is constrained by the shape of the gulf, then it forms a tidal bore; meanwhile, water from the Qiantang river makes the tidal stronger, as the outer water and the inner water block each other. Seawater flows into the Qiantang river continuously and another tidal bore is formed. In addition, the large scale of sand sediment and the higher bed river at the mouth are favorable to tidal bore.

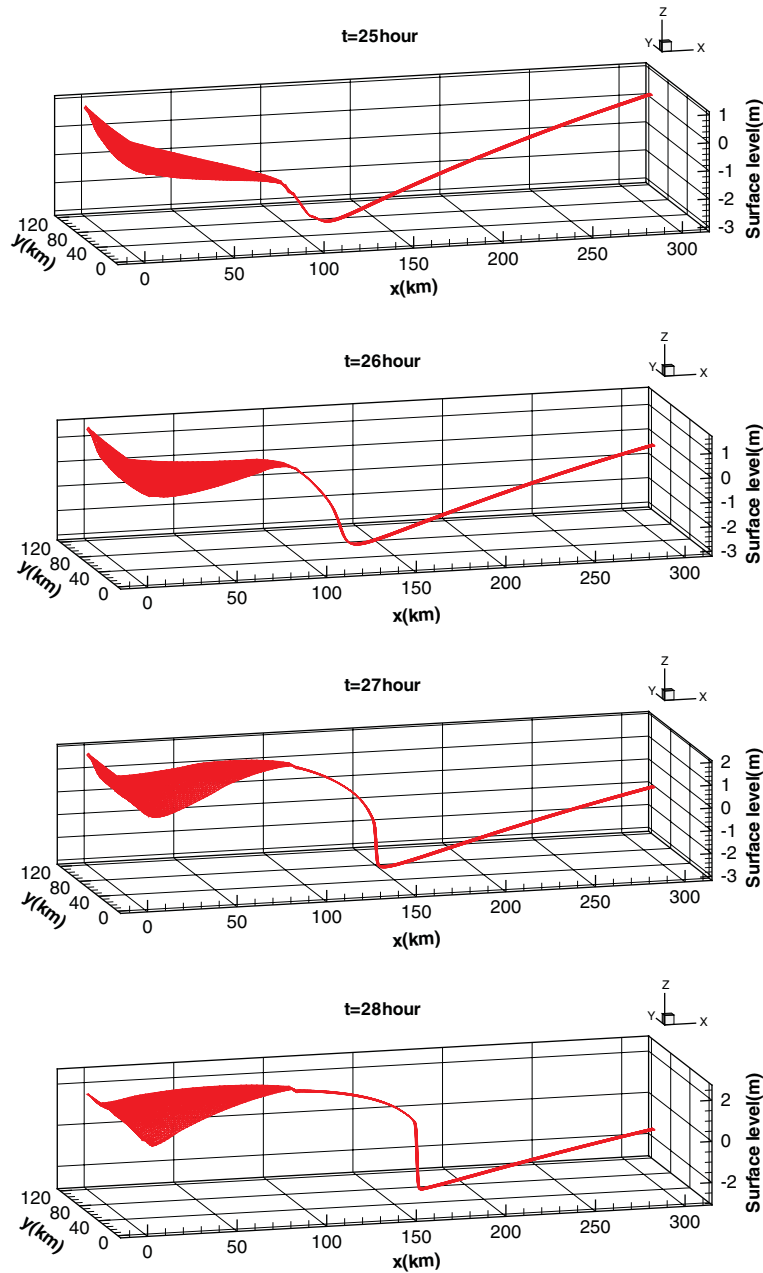Figure 8. The surface level of a trumpet estuary from $t=25$ to $t=32$ from top to bottom.

The calculated domain is from Ganpu to Cangqian in [6, 7, 9], where the tidal bore forms, evolves and dissipates, and the tributary named Cao'e river is ignored in [6, 9]; Pan *et al.* [7] generalized Cao'e river, while we keep it as its real shape.
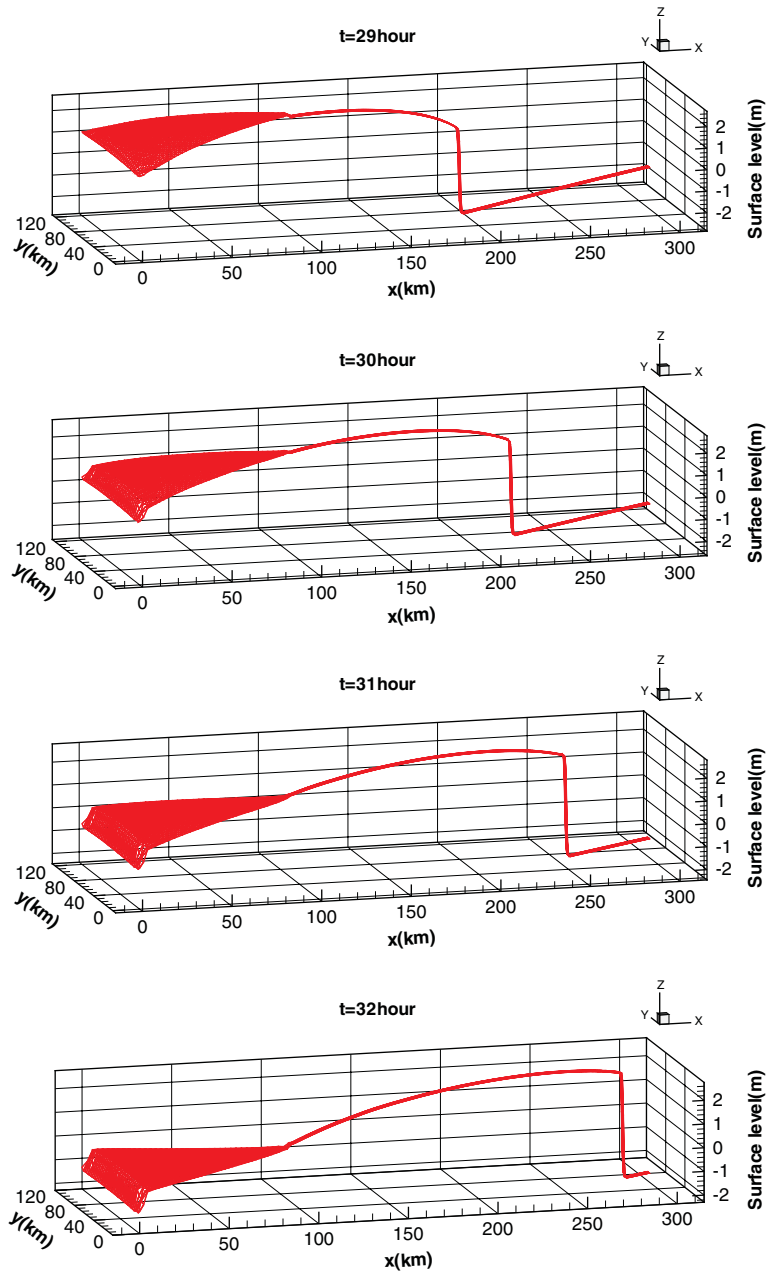
Figure 8. *Continued*.

There are isolated islands and shoals that outcrop over the water surface at ebb in the real bottom topography. We made it smooth in order to assure no great gradient of the bottom to operate the computation completely. The modified topography of bottom is shown in Figure 10.
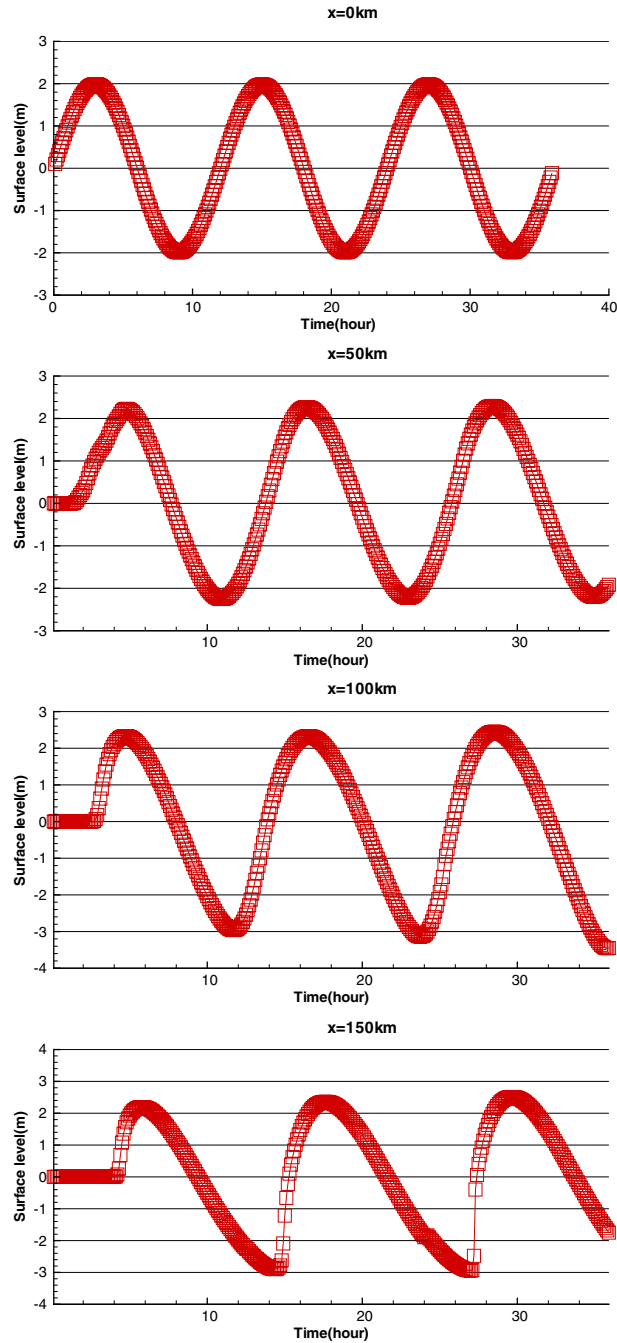
Figure 9. The distribution of the surface level with 360 data at $x = 0, 50, 100, 150, 200, 250, 300\,\text{km}$, respectively, for a trumpet estuary from top to bottom.
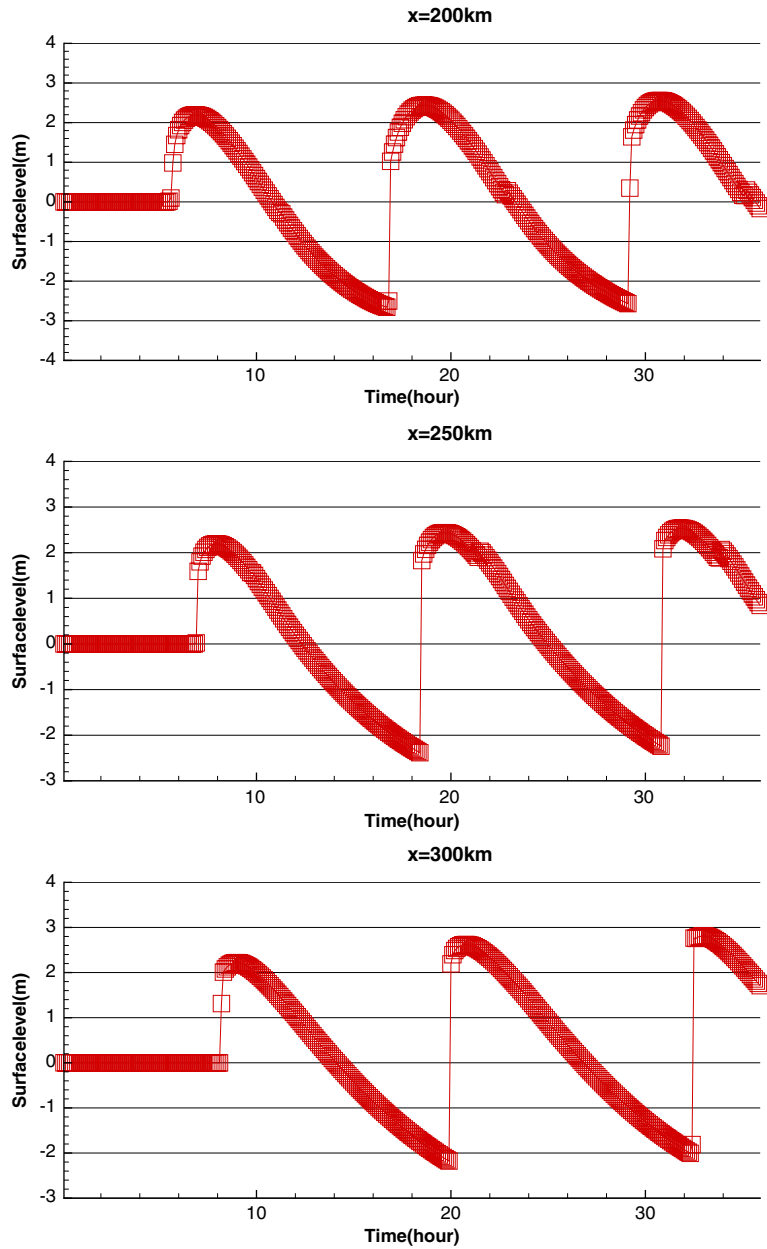
Figure 9. *Continued.*

The initial velocity and the free surface elevation above the still water level are set to be zero as the initial conditions. The reflection boundary condition is used for solid wall boundary. The water boundary of the tributary named Cao'e river is considered as the wall boundary because of the
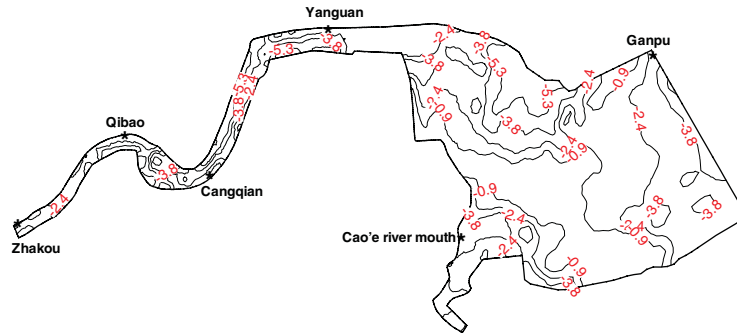
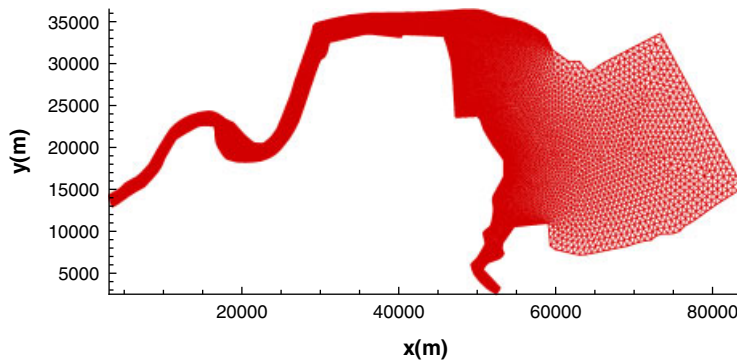Figure 10. The contours of modified bottom topography for Qiantang river.

Figure 11. Shape and meshes of Qiantang river.

small influence and lack of observed data. The observed water level of upstream and downstream is chosen as the water boundary condition, which was observed continuously during seven days on 22–28 October 2003. It was recorded at every hour by the stations. The timing observed free surface elevation of Yanguan (see Figure 10) in the calculated region is used for testing the scheme later.

In the computation, a mesh of 13 201 unstructured triangle cells with 3333 vertexes (see Figure 11) is used and the least scale of elements is about 100 m; the biggest scale is about 400 m. The Manning coefficient is 0.00001 for the flood tide and 0.002 for the ebb tide; the CFL number is 0.3.

The initial velocity u, v and the free surface elevation ζ above the still water level are set to be zero as the initial conditions. The results in the initial stage are affected by the initial conditions and ignored; here initial 12 h result is discarded.

The water boundary conditions at Ganpu (downstream) and Zhakou (upstream) [20] are shown in Figure 12; the label points of date mean the 0:00 on different days. We note that the mean water level is about 1 m at Ganpu and about 4 m at Zhakou, and the max tidal range is about 7 m at Ganpu and only 1.5 m at Zhakou during the 7 days.

As water flows inward, the rudimentary tidal bore is formed near Ganpu, and it becomes a clear tidal bore near Yanguan. The channel is straight near Yanguan; the trend of the tidal bore
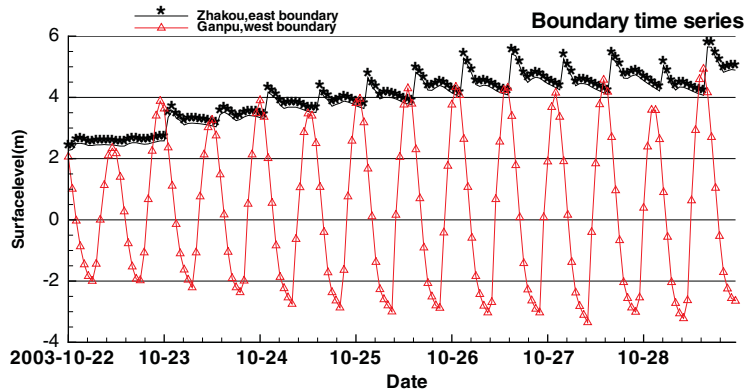
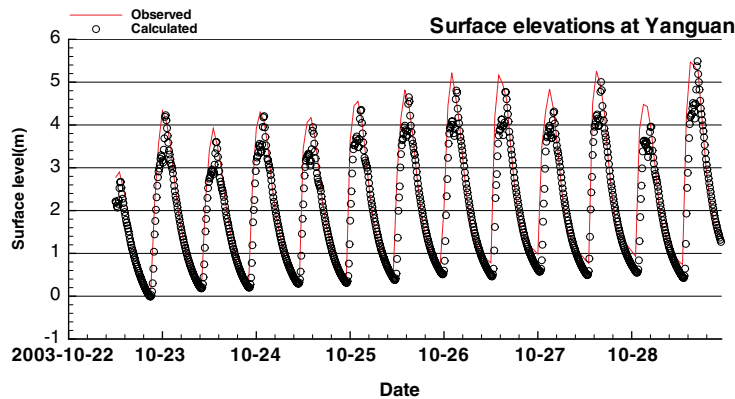Figure 12. Surface elevation boundary conditions at Ganpu and Zhakou.

Figure 13. Computed and measured surface elevations at Yanguan.

near Yanguan becomes uniform gradually, and it is called as 'a line-shaped tidal bore'. The reflection of the tidal bore appears in many places especially at corners when the tidal bore is stronger; this phenomenon is called as 'returning tidal bore'; then the strength of the tidal bore is slightly weakened, and the tidal range and the surface level fall down slowly near Daquekou. This phenomenon is coincident with the observation.

Although only the wet point is calculated, the results are consistent with measurement results approximately. The variance of water level at Yanguan can be calculated. In Figure 13, we compare the computed and observed variances of the free surface elevation [20], and they are found to be similar. In Figure 14, we show the computed flow velocity at Yanguan, the max velocity during flood more than -3 m/s, while ebb velocities are about 1.5 m/s. At the arrival and falling of the tidal bore, the velocity changed quickly; the phenomenon is similar to the result of Madsen *et al.* [9] and Pan *et al.* [7].
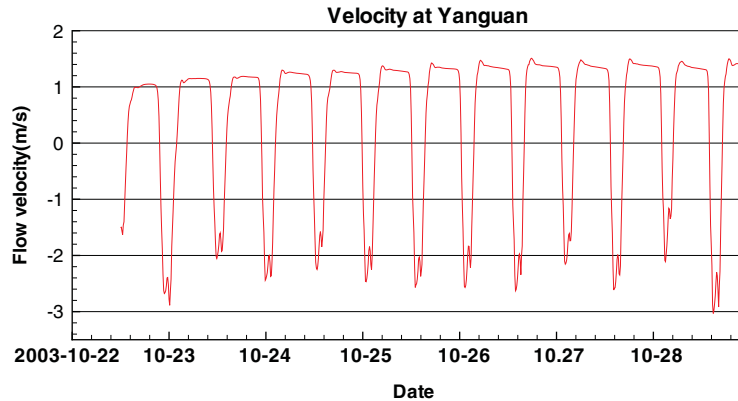
Figure 14. Computed velocity at Yanguan.

4. CONCLUDING REMARKS

In this paper, on the unstructured triangle mesh the WENO schemes are used to simulate the two-dimensional shallow water equations. The balance of the flux and the source terms makes the shallow water equations fit to the non-flat bottom problem. According to the tests of some typical examples and the simulation of a tidal bore on an estuary with trumpet shape and Qiantang river, the numerical results show that the WENO schemes can simulate the current flow accurately and catch the stronger discontinuous in water wave, such as dam break and tidal bore.

The tidal bore on an estuary with trumpet shape is computed with the schemes. The formation, development, propagation, and dissipation of Qiantang tidal bore are simulated successfully with the schemes. We can know more details about tidal bore and forecast it for guiding us in the planning and protection of Qiantang river.

REFERENCES

1. Tan WY, Han ZC. *Two Dimensional Numerical Simulation of the Tidal Bore in Hangzhou Gulf*. Nanjing Institute of Hydrology and Water Source, The Institute of Coast and Estuarine, 1993; 93–105.
2. Spitaleri RM, Corinaldesi L. A multigrid semi-implicit finite difference method for the two dimensional shallow water equations. *International Journal for Numerical Methods in Fluids* 1997; **25**:1229–1240.
3. Cai Y, Navon IM. Parallel block preconditioning techniques for the numerical simulation of the shallow water flow using finite element methods. *Journal of Computational Physics* 1995; **122**:39–50.
4. Liu XD, Osher S, Chan T. Weighted essentially non-oscillatory schemes. *Journal of Computational Physics* 1994; **115**:200–212.
5. Jiang GS, Shu CW. Efficient implementation of weighted ENO schemes. *Journal of Computational Physics* 1996; **126**:202–228.
6. Su MD, Xu X, Zhu JL, Hon YC. Numerical simulation of tidal bore in Hangzhou Gulf and Qiantangjiang. *International Journal for Numerical Methods in Fluids* 2001; **36**:205–247.
7. Pan CH, Lin B, Mao X. New development in the numerical simulation of the tidal bore. *Proceedings of the International Conference on Estuaries and Coasts*, Hangzhou, China, November 2003; 99–111.
8. Hui WH, Pan CH. Water level-bottom topography formulation for the shallow-water flow with application to the tidal bores of the Qiantang river. *Computational Fluid Dynamics Journal* 2003; **12**:549–554.
9. Madsen PA, Simonsen HJ, Pan CH. Numerical simulation of tidal bores and hydraulic jumps. *Coastal Engineering* 2005; **52**:409–433.

10. LeVeque RJ. Balancing source terms and flux gradients in high-resolution Godunov method: the quasi-steady wave-propagation algorithm. *Journal of Computational Physics* 1998; **346**:146.
11. Hubbard M, Garcia-Navarro P. Flux difference splitting and the balancing of source terms and flux gradients. *Journal of Computational Physics* 2000; **165**:89–125.
12. Zhou JG, Causon DM, Mingham CG, Ingram DM. The surface gradient method for the treatment of source terms in the shallow water equations. *Journal of Computational Physics* 2001; **168**:1–25.
13. Hu CQ, Shu CW. Weighted essentially non-oscillatory schemes on triangular meshes. *Journal of Computational Physics* 1999; **150**:97–127.
14. Rogers BD, Borthwick AGL, Taylor PH. Mathematical balancing of flux gradient and source terms prior to using Roe's approximate Riemann solver. *Journal of Computational Physics* 2003; **192**:422–451.
15. Shu CW. Total-variation-diminishing time discretizations. *SIAM Journal on Scientific Computing* 1988; **9**: 1073–1084.
16. Xing YL, Shu CW. High order finite difference WENO schemes with the exact conservation property for the shallow water equations. *Journal of Computational Physics* 2005; **208**:206–227.
17. Ricchiuto M, Abgrall R, Deconinck H. Application of conservative residual distribution schemes to the solution of the shallow water equations on unstructured meshes. *Journal of Computational Physics* 2007; **222**:287–331.
18. Anastasiou K, Chan CT. Solution of the 2D shallow water equations using the finite volume method on unstructured triangular meshes. *International Journal for Numerical Methods in Fluids* 1997; **24**:1225–1245.
19. Chleffi V, Valaini A, Zanni A. Finite volume method for simulating extreme flood events in natural channels. *Journal of Hydraulic Research* 2003; **41**:167–177.
20. Pan CH *et al.* Numerical simulation for 2D shallow water discontinuous flow. Research Report of Zhejiang Institute of Hydraulic & Estuary, 2006 (in Chinese).